Materials Today 100 (2026) 103497

Contents lists available at ScienceDirect

Materials Today

journal homepage: www.elsevier.com/locate/mattod

# Super ductile steel via sequentially activating multiple strengthening mechanisms

Yuanhong Liu [a], Si Gao [a,*], Myeong-heom Park [a], Shuhei Yoshida [a], Reza Gholizadeh [a], Zhenghao Chen [a], Keisuke Ikeda [b], Jin-Yu Zhang [c,d], Saeid Alipour [d], Jesada Punyafu [e], Wenqi Mao [f], Mitsuhiro Murayama [e,g], Kyosuke Kishida [a], Akinobu Shibata [h], Tomotsugu Shimokawa [b], Shigenobu Ogata [c], Ju Li [d,*], Nobuhiro Tsuji [a,*]

[a] *Department of Materials Science and Engineering, Kyoto University, Yoshida-honmachi, Sakyo-ku, Kyoto 606-8501, Japan*
[b] *Faculty of Mechanical Engineering, Kanazawa University, Ishikawa 920-1192, Japan*
[c] *Department of Mechanical Engineering and Bioengineering, Graduate School of Engineering Science, The University of Osaka, Toyonaka 560-8531, Japan*
[d] *Department of Nuclear Science and Engineering and Department of Materials Science and Engineering, MIT, Cambridge, MA, USA*
[e] *Institute for Materials Chemistry and Engineering, Kyushu University, Fukuoka 816-8580, Japan*
[f] *Key Laboratory of Electromagnetic Processing of Materials (Ministry of Education), Northeastern University, Shenyang 110819, China*
[g] *Department of Materials Science and Engineering, Virginia Tech, VA 24061, USA*
[h] *Research Center for Structural Materials, National Institute for Materials Science, 1-2-1 Sengen, Tsukuba, Ibaraki 305-0047, Japan*

A R T I C L E I N F O

*Keywords:*
Metals
Alloy
Mechanical properties
Strengthening mechanisms

A B S T R A C T

We report an Fe-24Ni-0.6C (*wt.*%) austenitic steel exhibiting a huge tensile uniform elongation of approximately 140 % and an extraordinary strength-ductility combination of 122 GPa%—record-breaking values that surpass all known structural metallic materials. These exceptional tensile properties arise from an intrinsically coordinated sequence of multiple deformation (strengthening) mechanisms—dislocation glide, deformation twinning and deformation-induced martensitic transformation—each activated approximately when the previous mechanism becomes insufficient to maintain uniform elongation. This temporally orchestrated transition sustains a high strain-hardening rate over an unusually wide strain range, thereby delaying necking and enabling huge tensile ductility and ultra-high strength (true tensile stress up to 2.1 GPa). This work has demonstrated a pathway-based strategy for maximizing strain-hardening capacity through temporally coordinated deformation modes, providing a mechanism-guided design principle for advanced structural alloys with exceptional strength–ductility synergy.

## Introduction

Strength and ductility play central roles in determining the mechanical performance of structural alloys. Strength enables load bearing, whereas ductility provides damage tolerance and energy absorption. However, improving one inevitably compromises the other, giving rise to the long-standing strength-ductility trade-off. This dilemma originates from the intrinsic coupling between material's strength and its strain hardening capacity. During tensile deformation, the uniform elongation is dictated by the plastic instability condition [1]: once the strain-hardening rate (SHR) falls below the flow stress, plastic instability (i.e., necking) initiates. In conventional metals of which plastic deformation is governed solely by dislocation slip, an initially high strain-hardening rate arises from rapid forest dislocation accumulation, but it progressively decays as the capacity of dislocation storage decreases with increasing strain, limiting uniform elongation to ~ 20–40 % in fully annealed alloys [2–4]. High-strength alloys—typically strengthened by grain refinement, cold work, or precipitation—tend to neck much earlier (~5–10 %) because their available strain-hardening capacity has been largely depleted prior to tensile loading [5–8].

To extend the limited strain-hardening capacity of dislocation-slip–dominated plasticity, advanced alloys increasingly exploit metastability engineering by introducing additional deformation mechanisms—most notably twinning-induced plasticity (TWIP) and transformation-induced plasticity (TRIP) [9,10]. By dynamically generating new interfaces (twin boundaries) or harder product phases

* Corresponding authors.
*E-mail addresses:* gao.si.8x@kyoto-u.ac.jp (S. Gao), liju@mit.edu (J. Li), nobuhiro-tsuji@mtl.kyoto-u.ac.jp (N. Tsuji).

https://doi.org/10.1016/j.mattod.2026.103497
Received 13 May 2026; Received in revised form 30 July 2026; Accepted 22 August 2026
Available online 1 September 2026

(strain-induced martensite) during deformation, these mechanisms can substantially enhance strain hardening and delay the onset of plastic instability [10]. Nevertheless, most existing strategies rely on a single dominant strengthening mechanism, and the attainable strength–ductility combination is consequently limited. Although integrating multiple deformation mechanisms (such as slip, twinning and martensitic transformation) to provide a larger overall strain-hardening potential and thereby achieve superior strength–ductility synergy appears highly promising in principle, effectively realizing such integration within a single alloy remains exceptionally challenging.

A major difficulty in integrating multiple deformation mechanisms arises from the strong coupling between the governing parameters of deformation twinning and martensitic transformation, most notably the stacking-fault energy (SFE) and phase stability of the parent phase, respectively [11]. These parameters often render the two mechanisms mutually competitive rather than cooperatively sequential, such that activating one tends to suppress the other [12]. Consequently, reported alloys that exhibit both twinning and transformation frequently rely on chemical or microstructural heterogeneities to locally vary SFE or phase stability, enabling different regions to deform by different mechanisms [13–15]. However, such spatial partitioning does not necessarily produce successive strain-hardening contributions within the same deforming microstructure. Another difficulty lies in achieving a well-timed sequential activation of deformation mechanisms: to maximize the strain-hardening contribution of each mechanism, the contribution of a subsequent mechanism should become significant as that of the preceding mechanisms become insufficient to prevent plastic instability [16]. Achieving such a delicate handover requires finely tuned control of SFE, phase stability, microstructural evolution during deformation—an exceptionally demanding requirement that has rarely been fulfilled. Consequently, the previously reported steels that exhibit both twinning and transformation have rarely demonstrated tensile properties exceeding those of conventional TWIP or TRIP steels [15,17,18].

Here we show that uniform elongation and strength–ductility synergy can be substantially enhanced by intrinsically sequential transitions among multiple deformation mechanisms rather than relying on a single dominant hardening source. To realize this principle, we design an Fe–24Ni–0.6C (wt.%) austenitic alloy that enables such temporally coordinated deformation. Detailed microstructural characterization and in-situ diffraction analyses reveal an intrinsically coordinated deformation pathway involving dislocation slip at low strains, deformation twinning at intermediate strains, and deformation-induced martensitic transformation at large strains. Each mechanism is approximately activated as the strain-hardening potential of the preceding mechanism approaches exhaustion, thereby sustaining a sufficiently high strain-hardening rate over an unusually wide strain range. This orchestrated deformation sequence leads to a huge uniform elongation of ~ 140 % together with an extraordinary strength–ductility product of 122 GPa% (uniform engineering strain × peak engineering stress), far exceeding values of previously reported structural metallic materials. These findings establish a pathway-based, mechanism-guided strategy for designing advanced structural alloys with exceptional strength–ductility synergy by maximizing strain-hardening capacity through temporally coordinated deformation modes.

## Results and discussion

An Fe–24Ni–0.6C (wt.%) austenitic steel was developed based on our previous research on the Fe-Ni-C austenitic TRIP steels [19,20]. The alloy was designed by increasing the carbon content to delay deformation-induced martensite and thereby open an intermediate strain window for deformation twinning, with the aim of achieving successive strain-hardening contributions from slip, TWIP, and TRIP. The detailed alloy-design rationale and comparisons with lower-carbon Fe–Ni–C alloys are provided in the **Supplementary materials**. A flat ingot with a mass of approximately 50 kg was produced by vacuum induction melting and casting. The as-cast ingot was subsequently processed by homogenization, conventional hot rolling, cold rolling and annealing (See **Supplementary materials** for details), yielding bulky material composed of equiaxed austenite grains with an average size of ~ 9 μm and weak texture (Fig. 1**A**). A representative tensile test revealed a yield strength of 240 MPa, an ultimate tensile strength of 900 MPa, an extraordinary uniform elongation of 136.3 % and a total elongation of 141.8 % (Fig. 1**B**). Fractography revealed full dimple patterns of the fracture surface, indicating the intrinsically ductile fracture behavior (Fig. 1**B** insets). Remarkably, the tensile ductility surpasses all previously reported metallic materials and is even twice that of TWIP steels (typically ~ 70 %) (Fig. 1**C**). Owing to the high strength and exceptional tensile ductility, the steel achieves a strength-ductility combination of 122 GPa% —the highest among all known metallic materials (Fig. 1**C**).

The superior strength-ductility synergy of the steel is attributed to its excellent strain hardening behavior, enabled by multiple strengthening mechanisms that sequentially activated during tensile deformation (Fig. 2**A**). At early stage (true strain $\varepsilon < 0.25$), plastic deformation was governed solely by dislocation slip (Fig. 2**B-① and C**), during which the strain-hardening rate (SHR) monotonically decreased with tensile true strain. This decay reflects the progressively reduced efficiency of dislocation storage due to enhanced dynamic recovery [46], as commonly observed in conventional metals. From $\varepsilon = 0.25$, however, the decline in SHR slowed down, and an inflection occurred at $\varepsilon = 0.34$. Deformation twins appeared at $\varepsilon = 0.26$ (Fig. 2**B-② and D**), and their density increased continuously with strain (Fig. 2**B-③ to B-④**). Each deformation twin consists of a bundle of nano-twins with individual lamella thicknesses of 50–160 nm (Fig. 2**E**), similar to those reported in classical TWIP steels [10]. The initiation and subsequent multiplication of deformation twins coincide with the transition in strain hardening behavior over $\varepsilon = 0.25$ to $\varepsilon = 0.40$, suggesting that the TWIP effect contributed significantly to renewed strain hardening.

Deformation-induced BCC martensite first appeared at $\varepsilon = 0.34$. Its fraction remained negligible up to $\varepsilon = 0.47$, during which deformation was still dominated by dislocation slip and deformation twinning (Fig. 2**B-③ to 2B-⑤**). Beyond this strain, however, the martensite fraction increased consistently, reaching ~ 30 % by $\varepsilon = 0.86$ (Fig. 2**B-⑥ to 2B-⑨**). This stage coincided with a gradual rise in the SHR, which stabilized at ~ 2500 MPa and enabled the steel to sustain uniform deformation up to $\varepsilon = 0.86$ (approximately 140 % in engineering strain) and reach an exceptional true tensile stress of 2.1 GPa, underscoring the crucial role of the TRIP effect in sustaining late-stage hardening. At $\varepsilon = 0.86$, the SHR curve eventually intersects with the true stress–strain curve, satisfying the Considère criterion ($d\sigma/d\varepsilon = \sigma$) and marking the onset of necking. A striking feature of this steel is that a large portion of the martensite nucleated within deformation twins of austenite, and its growth remained strictly confined within the twin bundles (Fig. 2**B-⑥ to 2B-⑨**). TEM observations (Fig. 2**F and G**) revealed that the martensite contained extremely fine BCC nano-twin substructures with a characteristic $\{112\}_{bcc}\ \langle 11\text{-}1\rangle_{bcc}$ twinning system and an average twin thickness of only ~ 2 nm. Such high carbon nano-twin martensite is expected to be exceptionally strong due to combined solid solution and twin-boundary strengthening [47], while the confinement imposed by the austenite twin bundles effectively suppresses the brittleness typically associated with coarse grained high-carbon martensite [47].

Quantitative EBSD analysis (Fig. 2**H**) provides deeper insight into the evolving interplay between deformation twinning and martensitic transformation. The area fraction of deformation twins increased continuously up to $\varepsilon = 0.53$, reaching ~ 11 %, but then appeared to decline slightly at higher strains. In contrast, the martensite fraction rose monotonically from 3 % to 31 % as the strain increased from $\varepsilon = 0.47$ to 0.86. Two distinct types of martensite were identified: one nucleating directly from the austenite matrix and another forming within deformation twins of austenite. The matrix-derived martensite initiated earlier ($\varepsilon \approx 0.47$–$0.53$) and soon saturated, while the twin-derived martensite dominated the subsequent stage up to fracture. The latter

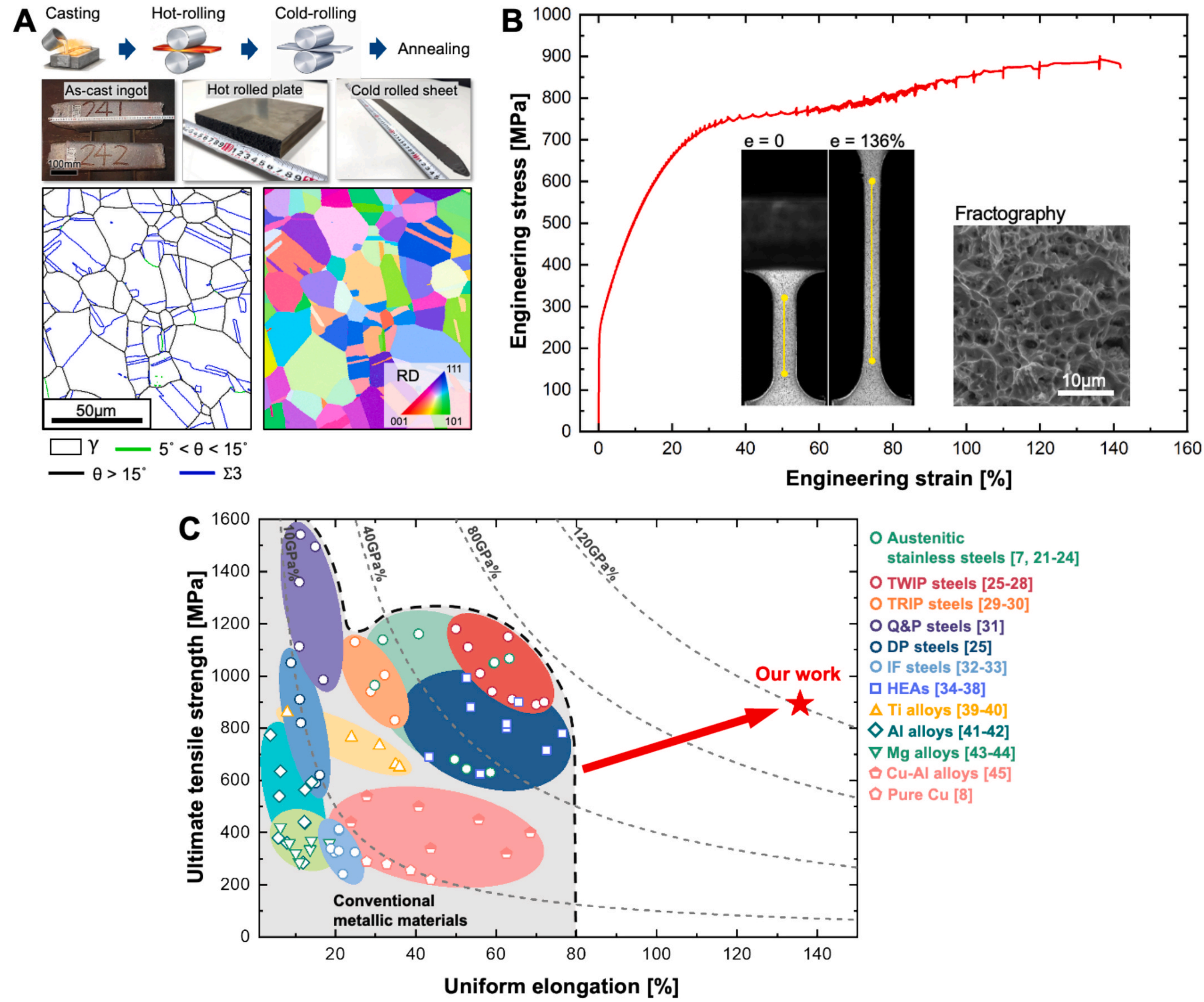


**Fig. 1. Microstructure and outstanding mechanical properties of the Fe-24Ni-0.6C steel.**
**(A)** Schematic illustration of the processing route of the steel, together with photographs of the as-cast ingot, hot-rolled plate, and cold-rolled thin sheet (upper). SEM-EBSD phase image plus grain boundary map (lower left) and inverse pole figure (IPF) map (lower right) displaying the initial microstructure of the Fe-24Ni-0.6C steel, showing a fully recrystallized austenitic structures with average grain size of ~ 9 μm and weak texture. **(B)** A representative tensile engineering stress–-strain curve, revealing a yield strength of 240 MPa, an ultimate tensile strength of 900 MPa, a uniform elongation of 136.3 %, and a total elongation of 141.8 %. Repeated tensile tests confirm the excellent reproducibility of the tensile response (**Supplementary materials Fig. S1** and **Table S2**). Insets: tensile specimen before deformation and right before tensile failure (left); Fractography (right) showing a ductile dimple morphology. **(C)** Comparison of the tensile properties of the present steel with a wide range of engineering alloys, demonstrating its exceptional strength-ductility synergy [7,8,21–45].

transformation effectively consumed the twinned regions, giving the apparent decrease in the measured twin fraction beyond $\varepsilon = 0.54$. Importantly, this apparent decline does not imply a cessation of twinning. Instead, the continued formation of new twins was dynamically balanced—and eventually overshadowed—by their conversion into martensite. Thus, deformation twinning remained active during the later deformation stage, continuously supplying precursor structures for transformation-induced strain hardening.

These results demonstrate that dislocation slip, TWIP, and TRIP were sequentially activated at different deformation stages, with each mechanism enhancing strain hardening up to tensile fracture. The predominant nucleation of martensite within deformation twins demonstrates that the TWIP → TRIP sequence was realized in both temporal and spatial terms.

We performed the tensile test with *in-situ* synchrotron X-ray diffraction to quantitatively evaluate the contribution of the different strengthening mechanisms (see **Supplementary materials** for the detailed analytical procedures). Fig. 3**A** shows the evolution of phase fractions: martensite first appeared at $\varepsilon = 0.48$ and increased steadily to 42 % by $\varepsilon = 0.83$, consistent with the microstructure observation in Fig. 2. The corresponding phase stresses of austenite and martensite, derived from diffraction peak shifts, are shown in Fig. 3**B**. Before martensitic transformation, the phase stress (i.e., the average elastic stress borne by each phase) of austenite essentially matched the macroscopic flow stress. Martensite exhibited an initial phase stress of ~ 1000 MPa, which significantly increased to ~ 3400 MPa before fracture. In contrast, the phase stress of austenite increased from ~ 1200 MPa to 1490 MPa and remained below the global flow stress. These results reveal a pronounced stress partitioning behavior [19] between the soft austenite and much harder martensite.

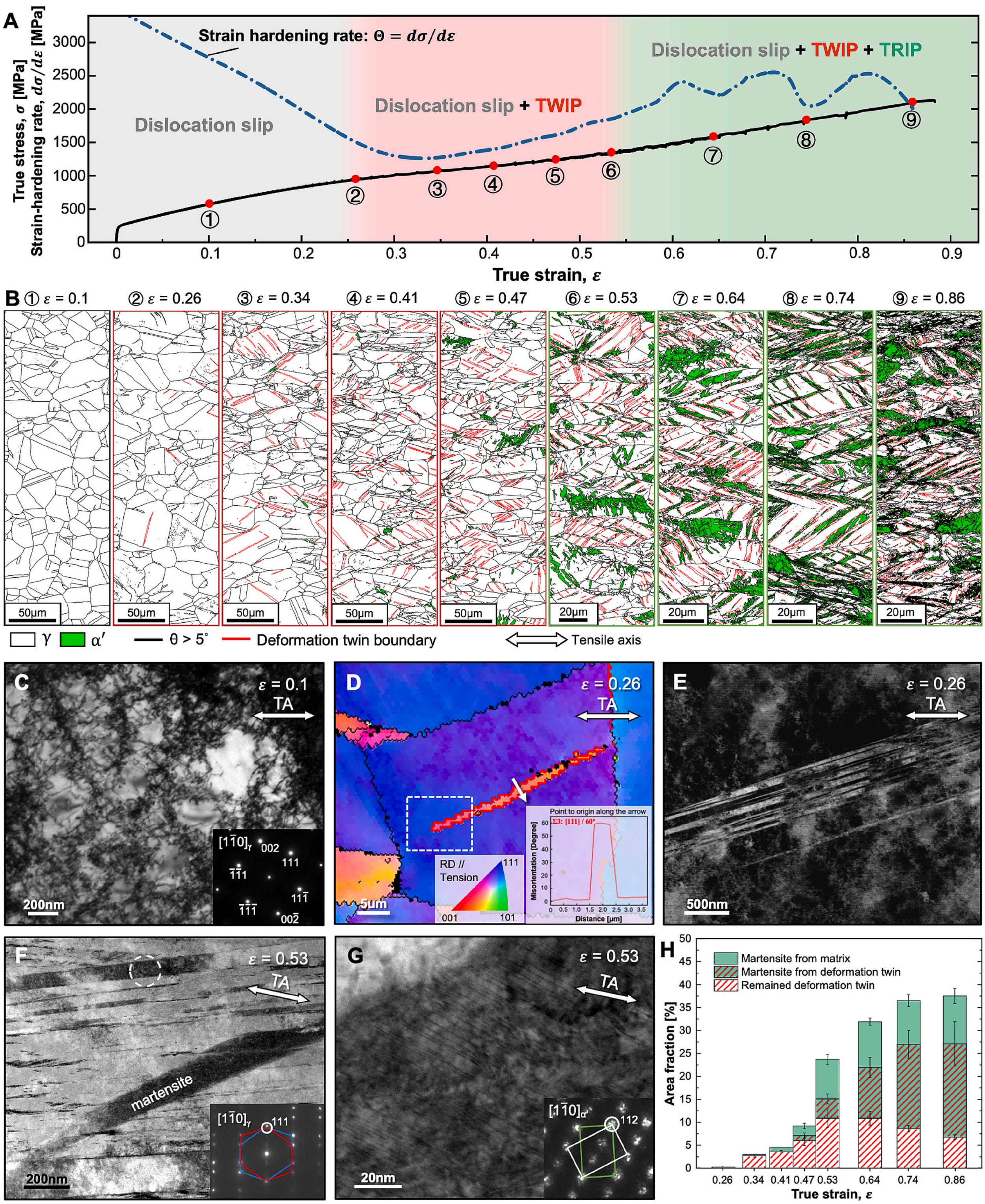


**Fig. 2. Microstructures evolution during tensile deformation of the Fe-24Ni-0.6C steel.**
**(A)** True stress–strain and strain-hardening rate (SHR) curves. **(B)** SEM-EBSD phase map plus grain boundary maps at true strains from 0.1 to 0.86. FCC austenite and deformation-induced BCC martensite are shown in white and green, respectively, and FCC deformation twin boundaries are highlighted in red. **(C)** TEM-BF image showing dislocation cell structures at true strain of 0.1. **(D)** SEM-EBSD grain boundary map and IPF map at a true strain of 0.26, showing a deformation twin within an austenite grain. The misorientation profile across the twin (inset) confirms a Σ3 twinning relationship. **(E)** SEM-ECC image of the region highlighted by the dashed box in (D), showing the FCC deformation twin composed of bundled nanotwins **(F)** STEM-BF image showing deformation-induced martensite formed within FCC deformation twins at a true strain of 0.53. Inset: selected-area diffraction (SAD) pattern confirming the Σ3 twinning relationship. **(G)** STEM-BF image and nano beam electron diffraction (NBED) patterns of deformation-induced BCC martensite, revealing the $\{112\}_{bcc}$ $\langle 11\text{-}1\rangle_{bcc}$ nano-twin substructures. **(H)** Evolution of area fractions of FCC deformation twins and martensite during tensile deformation. The martensite fraction consists of two contributions: one transformed directly from austenite matrix and another from the FCC deformation twins, with the latter being dominant at higher strains.

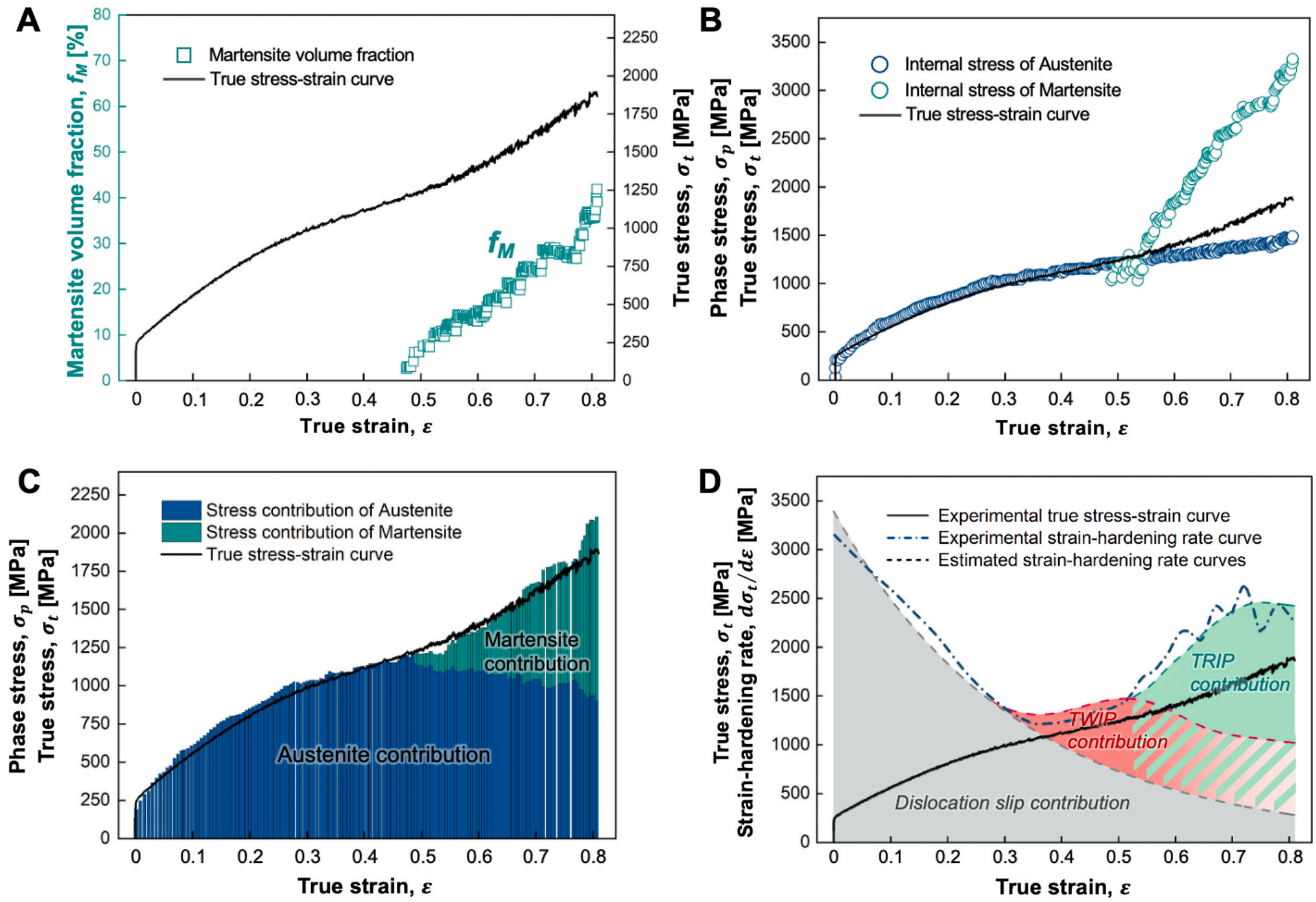


**Fig. 3. In-situ synchrotron X-ray diffraction measurement on the tensile deformation behavior of Fe-24Ni-0.6C steel.**
**(A)** Volume fraction of deformation-induced martensite as a function of global true strain. **(B)** Phase stresses of austenite and martensite as a function of global true strain. **(C)** Contributions of the austenite and martensite phase to the global flow stress. **(D)** Contributions of dislocation slip, twinning and martensitic transformation to the global strain-hardening rate.

The high phase stress of martensite (over 3 GPa) demonstrates its high load-bearing capacity and is consistent with the combined effects of carbon solid-solution strengthening and its nano-twinned substructure. By combining phase stresses with phase fractions, we further evaluated the respective contributions of austenite and martensite to the global flow stress (Fig. 3**C**). A significant contribution of martensite at the late stage of tensile deformation is observed, owing to the simultaneous increase in its phase stress and volume fraction.

We further estimated the respective contributions of forest dislocation hardening, deformation twinning, and martensitic transformation to the global SHR using the evolutions of phase stress, phase fraction, and dislocation density obtained from the *in-situ* XRD (See **Supplementary materials** for details). As shown in Fig. 3**D**, if only forest hardening were active, the SHR would decrease monotonically, and plastic instability (necking) would occur at $\varepsilon \approx 0.38$. Nonetheless, TWIP was activated at $\varepsilon \approx 0.30$ — approximately when forest hardening alone was about to become insufficient — and restored the SHR, extending the uniform strain to $\varepsilon \approx 0.60$. At $\varepsilon \approx 0.53$, when the combined hardening from dislocation slip and twinning was again nearly exhausted for maintaining uniform elongation, TRIP was triggered, further enhancing the SHR and pushing the onset of plastic instability to significantly higher strains. The predicted uniform elongations — 45 % for forest hardening alone and 70 % for forest hardening + TWIP—match the upper limits reported for conventional FCC metals and TWIP steels [48–51], indicating that the hardening potential of each mechanism was effectively used to delay necking. This critically timed activation—where each mechanism is triggered approximately when the preceding one is about to become insufficient—ensures that the strain-hardening potential of each mechanism is fully utilized, resulting in the alloy's exceptional strength-ductility synergy.

The evolutions of crystallographic orientation and microstructures in austenite during deformation collectively establish the pathway for the sequential activation of twins and martensite (Fig. 4). Prior to deformation, the grains displayed a weak $\langle 112\rangle_{fcc}$ // tensile axis (TA) texture characteristic of cold-rolled and annealed FCC metals (Fig. 4**A**) [52]. As deformation progressed, slip-induced grain rotation produced a strong $\langle 111\rangle_{fcc}$ // TA texture together with a weaker $\langle 001\rangle_{fcc}$ // TA component (Fig. 4**B**). Deformation twins appeared predominantly in the $\langle 111\rangle$ grains (Fig. 4**B and 4C**), where the Schmid factor is higher for the $\{111\}_{fcc}\langle 11\text{-}2\rangle_{fcc}$ slip system of Shockley partial dislocations — also the essential shear system for twinning [53] — than for the perfect dislocation slip (**Fig. S6**). Remarkably, the deformation twins reoriented into near $\langle 001\rangle_{fcc}$ // TA, the exact orientation with the highest Schmid factor for the martensitic transformation shear (**Fig. S6**). Consequently, both the $\langle 001\rangle$-oriented twins and matrix grains provided favorable sites for martensite nucleation during subsequent deformation (Fig. 4**D**). Our molecular dynamics (MD) simulations further elucidate this sequence (Fig. 4**E**). In the $\langle 111\rangle_{fcc}$ // TA grains, plastic deformation occurs by partial dislocation slip at a high tensile stress level, which explains the formation of deformation twinning at a relatively late strain stage in the $\langle 111\rangle$ grains. For martensite transformation, the nucleation stress is ordered as $\langle 111\rangle_{fcc}$ // TA > $\langle 100\rangle_{fcc}$ // TA matrix grains > $\langle 100\rangle_{fcc}$ // TA

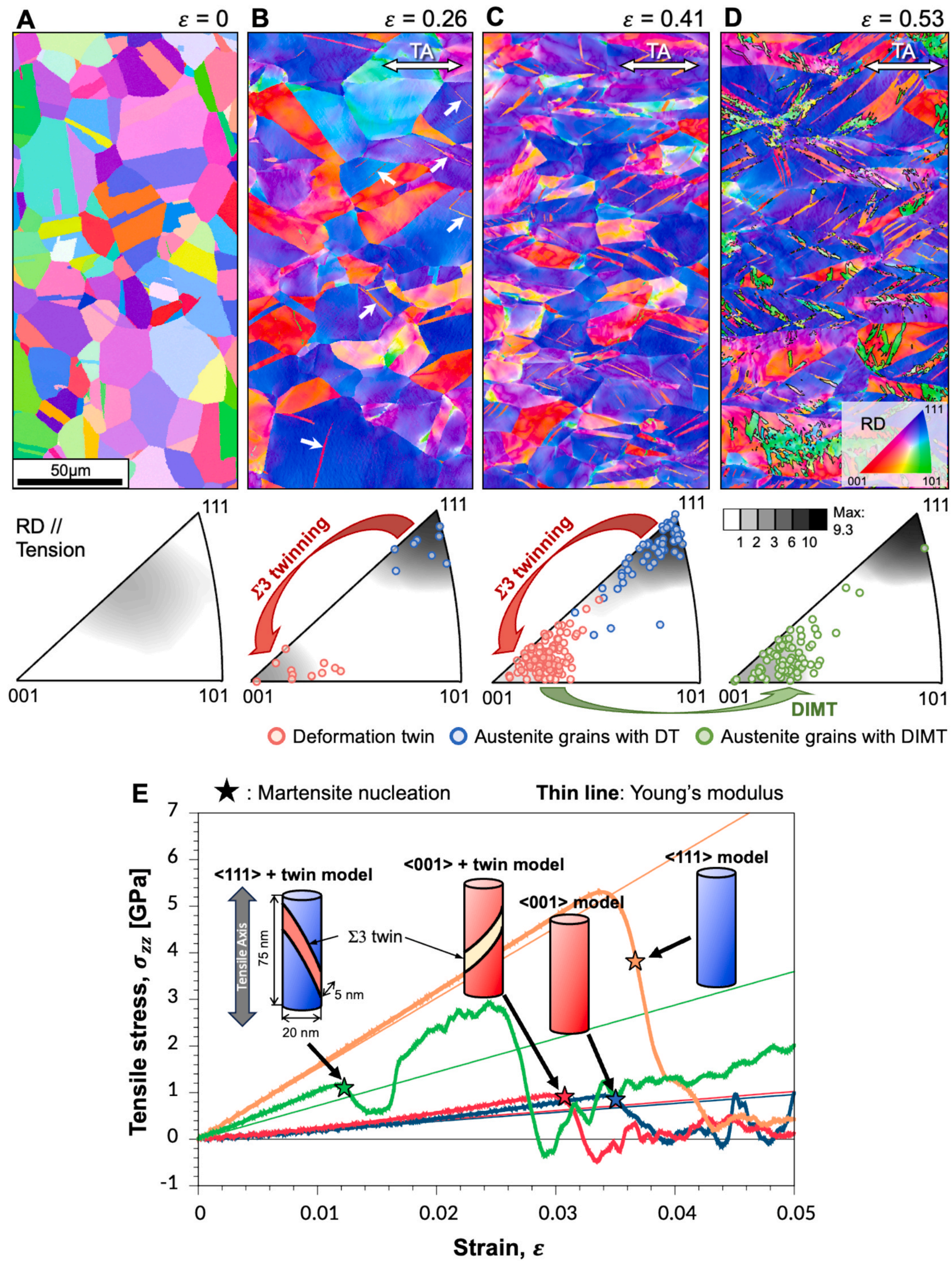


**Fig. 4. Orientation dependences of deformation twinning and deformation-induced martensite transformation.**
Inverse pole figure maps for specimen before tensile test **(A)** and deformed to **(B)** 0.26, **(C)** 0.41, and **(D)** 0.53 tensile true strains. The corresponding inverse pole figures are shown below and projected along TA in the scanning area. **(E)** Molecular dynamics simulations of the tensile stress–strain behavior of FCC pure iron were performed for four different models: tensile loading along the $\langle 001\rangle_{fcc}$ and $\langle 111\rangle_{fcc}$ crystallographic orientations, both with and without a pre-existing Σ3 twin. The observed stress drop corresponds to the onset of DIMT.

twin grains, consistent with preferential formation of martensite observed experimentally. The simulations also show that in $\langle 100\rangle_{fcc}$ // TA twin grain, the martensite preferentially nucleates at the twin boundaries, implying that twin boundaries themselves also promote martensitic transformation in addition to the orientation preference (**Fig. S10**). This crystallographic- and defect-mediated pathway — grain rotation to $\langle 111\rangle$, twinning within those grains, and subsequent martensite formation in the twins assisted by twin boundaries — underpins the sequential activation of dislocation slip, TWIP and TRIP.

Our findings show that carbon plays a critical role in enabling the sequential pathway of dislocation slip → TWIP → TRIP in the alloy. Although carbon is known to raise the SFE of austenite and suppress deformation twinning [17,54], the present 0.6C alloy exhibits abundant twinning, contrary to SFE-based expectations. Our density functional theory calculations (See Supplementary text for details) confirm that increasing the carbon content from 0.3 wt.% to 0.6 wt.% significantly increases the SFE (**Fig. S9**), and the WBDF-TEM observations further indicate a high-SFE state in which the dissociation of the Shockley partials cannot be resolved due to the extremely narrow dissociation width (< 2 nm) (**Fig. S8**). These findings indicate that the extensive twinning in the 0.6C alloy cannot be rationalized solely based on its SFE. Besides the intrinsic SFE, sufficiently high local stresses can also activate twinning by enabling the nucleation of Shockley partial dislocations in high-SFE alloys [55]. Similar deviations from conventional SFE-based expectations have been reported in high-carbon austenitic steels [56–58]. In these alloys, dynamic strain aging has been proposed to assist deformation twinning through interactions between interstitial carbon and extended dislocations [56–58]. In particular, preferential pinning of the trailing partial may increase the effective separation between the leading and trailing partials, thereby stabilizing the stacking-fault ribbon and facilitating successive partial-dislocation activity on adjacent {111} planes required for twin nucleation. This mechanism provides a possible explanation for the occurrence of deformation twinning even when the intrinsic SFE is relatively high. The high carbon content and flow-stress serrations of the present steel are consistent with dynamic strain aging. However, whether DSA directly assists deformation twinning cannot be conclusively established from the present results and requires further investigation.

Carbon also strongly governs the activation and kinetics of subsequent deformation mechanisms, thereby maintaining a high strain-hardening rate over a wide strain range. By stabilizing austenite, carbon postpones the onset of martensitic transformation and slows its kinetics, enabling the TRIP effect to develop progressively under substantial strains rather than abruptly at early stages. Meanwhile, the martensite formed in the 0.6C alloy exhibits a high load-bearing capacity, consistent with the combined effects of carbon solid-solution strengthening and its nano-twinned substructure. Its fine and constrained distribution within the pre-existing deformation-twin bundles also helps avoid premature brittle fracture. Through this combination—facilitating twinning despite high SFE, delaying but strengthening TRIP, and coordinating the timing of each mechanism—carbon enables the precise sequencing of dislocation slip → TWIP → TRIP, which in turn sustains a favorable strain-hardening rate across an unusually wide strain range and yielding the remarkable ductility of this alloy.

To quantitatively assess the role of carbon in controlling the deformation pathway, we compared the present alloy with our previously investigated Fe–24Ni–0.3C (wt.%) alloy (**Fig. S12**), which has the same Ni content but a lower carbon content. The Fe–24Ni–0.3C alloy exhibits conventional early-stage TRIP behavior: DIMT begins at a true strain of approximately 0.16, reaches a martensite fraction of approximately 72 % before necking, and is not accompanied by detectable deformation twinning. In contrast, in the present Fe–24Ni–0.6C alloy, deformation twinning becomes active at a true strain of approximately 0.26, whereas pronounced DIMT is delayed to approximately 0.47 true strain, with the martensite fraction reaching approximately 40 % near the onset of necking. Thus, increasing the carbon content from 0.3 to 0.6 wt.% at a fixed Ni content substantially suppresses early-stage DIMT and opens an intermediate strain regime in which deformation twinning can operate, thereby changing the deformation pathway from conventional early-stage slip–TRIP behavior to the intended slip–TWIP–TRIP sequence. A detailed comparison is provided in the **Supplementary materials.**

The sequential activation behavior is expected to be influenced by both microstructural factors and external conditions. For example, grain refinement or increasing the deformation temperature enhances the mechanical stability of austenite and increases the critical stresses for both deformation twinning and DIMT, thereby increasing their onset strains and reducing their kinetics. Strain rate may affect the sequence through competing effects of increased flow stress and adiabatic heating. Therefore, achieving the desired sequential activation requires the coordinated control of alloy composition, microstructure, and testing conditions to establish an appropriate processing window, in which the onset strains and kinetics of the individual deformation mechanisms are properly balanced to sustain strain hardening and optimize the strength–ductility combination.

## Conclusion

In summary, we demonstrate that an Fe-24Ni-0.6C (wt.%) austenitic steel exhibits an unprecedented uniform elongation of nearly 140 % together with a strength and ductility combination of 122 GPa%, surpassing all previously reported metallic materials. This extraordinary strength-ductility synergy originates from the sequential activation of dislocation slip, deformation twinning, and martensitic transformation, which collectively sustain a sufficiently high strain-hardening rate spread across a wide strain range. These findings establish a mechanism-guided strategy for maximizing strain-hardening efficiency through intrinsic sequential activation of multiple deformation mechanisms, offering a potentially applicable design principle for developing novel structural alloys with exceptional combinations of strength and ductility.

## CRediT authorship contribution statement

**Yuanhong Liu:** Writing – review & editing, Writing – original draft, Investigation, Formal analysis, Data curation. **Si Gao:** Writing – review & editing, Writing – original draft, Supervision, Investigation, Funding acquisition, Formal analysis, Conceptualization. **Myeong-heom Park:** Writing – review & editing, Investigation, Funding acquisition, Formal analysis. **Shuhei Yoshida:** Writing – review & editing, Investigation, Funding acquisition, Formal analysis. **Reza Gholizadeh:** Writing – review & editing, Investigation, Formal analysis. **Zhenghao Chen:** Writing – review & editing, Formal analysis, Data curation. **Keisuke Ikeda:** Writing – review & editing, Formal analysis, Data curation. **Jin-Yu Zhang:** Writing – review & editing, Formal analysis, Data curation. **Saeid Alipour:** Writing – review & editing, Formal analysis, Data curation. **Jesada Punyafu:** Writing – review & editing, Formal analysis, Data curation. **Wenqi Mao:** Writing – review & editing, Investigation, Formal analysis. **Mitsuhiro Murayama:** Writing – review & editing, Investigation, Formal analysis, Data curation. **Kyosuke Kishida:** Writing – review & editing, Investigation, Formal analysis. **Akinobu Shibata:** Writing – review & editing, Investigation, Formal analysis. **Tomotsugu Shimokawa:** Writing – review & editing, Formal analysis, Data curation. **Shigenobu Ogata:** Writing – review & editing, Investigation, Formal analysis. **Ju Li:** Writing – review & editing, Writing – original draft, Investigation, Formal analysis, Data curation. **Nobuhiro Tsuji:** Writing – review & editing, Writing – original draft, Supervision, Project administration, Funding acquisition, Conceptualization.

## Declaration of competing interest

The authors declare that they have no known competing financial interests or personal relationships that could have appeared to influence the work reported in this paper.

## Acknowledgments

**N.T** and **S.G** acknowledge financial support from Japan Science and Technology Agency (JST) through the CREST program (Grant No. JPMJCR1994), the Japan Society for the Promotion of Science (JSPS) through the fund for the Promotion of Joint International Research (International Leading Research) (Grant No. JP23K20037) and JSPS KAKENHI (Grant Nos.25K08343, and 22K14509). **Y.L** acknowledges the financial support from China Scholarship Council (CSC), China. The synchrotron radiation experiments (beam-time number 2023A1038, 2023A1823, 2024A1668) at SPring–8 were performed with the approval of the Japan Synchrotron Radiation Research Institute (JASRI). **J-Y.Z**, **S. O,** and **J.L** acknowledge financial support from JSPS KAKENHI (No.

JP23K20037). **N.T** and **S.G** designed and supervised the study. **Y.L** prepared the material and conducted experiments on mechanical testing and microstructure observations. **J.P**, **Z.C**, **S.Y**, **R.G** and **M.M** conducted TEM characterizations and analysis. **W.M** assisted with the synchrotron XRD data analysis. **K.I** and **T.S** conducted Molecular Dynamics simulations. **J-Y.Z**, **S.A**, **S.O** and **J.L** performed Density Functional Theory calculations. **A.S** guided the crystallography analysis. **Y.L** and **S.G** wrote the draft of the manuscript. All authors contributed to the discussion on the results and the revision on the manuscript.

## Appendix A. Supplementary data

Supplementary data to this article can be found online at https://doi.org/10.1016/j.mattod.2026.103497.

## Data availability

Data will be made available on request.

## References

[1] A. Considère, Annales des Ponts et Chaussées, Ann. Ponts Chaussees 9 (1885) 574.
[2] B. Devincret, L.P. Kubint, Simulations of forest interactions and strain hardening in FCC crystals, Modell. Simul. Mater. Sci. Eng. 2 (1994) 559–570.
[3] H. Li, et al., Mechanical response of dislocation interaction with grain boundary in ultrafine-grained interstitial-free steel, Acta Mater. 206 (2021) 116621.
[4] Y.Z. Tian, et al., Revealing the deformation mechanisms of Cu–Al alloys with high strength and good ductility, Acta Mater. 110 (2016) 61–72.
[5] N. Tsuji, et al., Strength and ductility of ultrafine grained aluminum and iron produced by ARB and annealing, Scr. Mater. 47 (2002) 893–899.
[6] N. Tsuji, et al., Ultra-fine grained bulk steel produced by accumulative roll-bonding (ARB) process, Scr. Mater. 40 (1999) 795–800.
[7] M. Liu, et al., Achieving excellent mechanical properties in type 316 stainless steel by tailoring grain size in homogeneously recovered or recrystallized nanostructures, Acta Mater. 226 (2022) 117629.
[8] Y.Z. Tian, et al., Two-stage Hall-Petch relationship in Cu with recrystallized structure, J. Mater. Sci. Technol. 48 (2020) 31–35.
[9] I. Tamura, Deformation-induced martensitic transformation and transformation-induced plasticity in steels, Metal Science 16 (1982) 245–253.
[10] B.C. De Cooman, Y. Estrin, S.K. Kim, Twinning-induced plasticity (TWIP) steels, Acta Mater. 142 (2018) 283–362.
[11] E.I. Galindo-Nava, P.E.J. Rivera-Díaz-del-Castillo, Understanding martensite and twin formation in austenitic steels: a model describing TRIP and TWIP effects, Acta Mater. 128 (2017) 120–134.
[12] S. Allain, et al., Correlations between the calculated stacking fault energy and the plasticity mechanisms in Fe-Mn-C alloys, Mater. Sci. Eng. A 387 (2004) 158–162.
[13] M.M. Wang, et al., Smaller is less stable: size effects on twinning vs. transformation of reverted austenite in TRIP-maraging steels, Acta Mater. 79 (2014) 268–281.
[14] J. Zhang, et al., Achieving heterogeneous TWIP/TRIP steel with 1GPa strength and 72% ductility by introducing austenite + martensite lamella structure, Mater Charact 197 (2023) 112709.
[15] H.W. Yen, et al., Role of stress-assisted martensite in the design of strong ultrafine-grained duplex steels, Acta Mater. 82 (2015) 100–114.
[16] N. Tsuji, et al., Strategy for managing both high strength and large ductility in structural materials–sequential nucleation of different deformation modes based on a concept of plaston, Scr. Mater. 181 (2020) 35–42.
[17] S. Martin, et al., Deformation mechanisms in austenitic TRIP/TWIP steel as a function of temperature, Metall. Mater. Trans. A 47 (2016) 49–58.
[18] S. Lee, Y. Estrin, B.C. De Cooman, Effect of the strain rate on the TRIP-TWIP transition in austenitic Fe-12 pct Mn-0.6 pct C TWIP Steel, Metall. Mater. Trans. A 45 (2014) 717–730.
[19] W. Mao, et al., Quantitatively evaluating respective contribution of austenite and deformation-induced martensite to flow stress, plastic strain, and strain hardening rate in tensile deformed TRIP steel, Acta Mater. 256 (2023) 119139.
[20] W. Mao, et al., In situ neutron diffraction revealing the achievement of excellent combination of strength and ductility in metastable austenitic steel by grain refinement, J. Mater. Sci. Technol. 176 (2024) 69–82.
[21] D.Y. Ryoo, N. Kang, C.Y. Kang, Effect of Ni content on the tensile properties and strain-induced martensite transformation for 304 stainless steel, Mater. Sci. Eng. A 528 (2011) 2277–2281.
[22] D.M. Xu, et al., Deformation behavior of high yield strength – high ductility ultrafine-grained 316LN austenitic stainless steel, Mater. Sci. Eng. A 688 (2017) 407–415.
[23] A. Kisko, et al., Effects of reversion and recrystallization on microstructure and mechanical properties of Nb-alloyed low-Ni high-Mn austenitic stainless steels, Mater. Sci. Eng. A 657 (2016) 359–370.
[24] M.C. Somani, et al., Enhanced mechanical properties through reversion in metastable austenitic stainless steels, Metall. Mater. Trans. A 40 (2009) 729–744.
[25] O. Bouaziz, H. Zurob, M. Huang, Driving force and logic of development of advanced high strength steels for automotive applications, Steel Res. Int. 84 (2013) 937–947.
[26] S. Hwang, M. Heom Park, Y. Bai, A. Shibata, W. Mao, H. Adachi, M. Sato, N. Tsuji, Mesoscopic nature of serration behavior in high-Mn austenitic steel, Acta Mater. 205 (2021) 116543.
[27] P. Lan, J. Zhang, Tensile property and microstructure of Fe-22Mn-0.5C TWIP steel, Mater. Sci. Eng. A 707 (2017) 373–382.
[28] M. Madivala, W. Bleck, Strain rate dependent mechanical properties of TWIP steel, JOM 71 (2019) 1291–1302.
[29] Z. Zeng, et al., Microstructure and mechanical properties of Nb and Ti microalloyed lightweight δ-TRIP steel, Mater Charact 164 (2020).
[30] J.Y. Lee, et al., The effect of austenite grain size on deformation mechanism of Fe–17Mn steel, Mater. Sci. Eng. A 809 (2021) 140972.
[31] E. De Moor, et al., Effect of carbon and manganese on the quenching and partitioning response of CMnSi steels, ISIJ Int. 51 (2011) 137–144.
[32] Y. Shadangi, K. Chattopadhyay, V. Singh, Microstructural modification and tensile behavior of IF steel processed through surface mechanical attrition treatment, JOM 72 (2020) 4330–4339.
[33] S. Mukherjee, et al., Insitu investigation of tensile deformation behaviour of cold-rolled interstitial-free high-strength steel in scanning electron microscope, Mater. Sci. Eng. A 776 (2020) 139029.
[34] Z. Li, et al., Metastable high-entropy dual-phase alloys overcome the strength-ductility trade-off, Nature 534 (2016) 227–230.
[35] P. Sathiyamoorthi, et al., Fine tuning of tensile properties in CrCoNi medium entropy alloy through cold rolling and annealing, Intermetallics 113 (2019) 106578.
[36] P. Wu, et al., Unexpected sluggish martensitic transformation in a strong and super-ductile high-entropy alloy of ultralow stacking fault energy, Acta Mater. 261 (2023) 119389.
[37] Z. Pei, et al., Theory-guided design of high-entropy alloys with enhanced strength-ductility synergy, Nat. Commun. 14 (2023).
[38] Q. Pan, et al., Gradient cell-structured high-entropy alloy with exceptional strength and ductility, Science 374 (2021) 984–989.
[39] S.H. Kim, H. Kim, N.J. Kim, Brittle intermetallic compound makes ultrastrong low-density steel with large ductility, Nature 518 (2015) 77–79.
[40] G. Zhao, X. Li, N. Petrinic, Materials information and mechanical response of TRIP/TWIP Ti alloys, npj Comput. Mater. 7 (2021) 91.
[41] K. Ma, et al., Mechanical behavior and strengthening mechanisms in ultrafine grain precipitation-strengthened aluminum alloy, Acta Mater. 62 (2014) 141–155.
[42] T. Aoba, M. Kobayashi, H. Miura, Effects of aging on mechanical properties and microstructure of multi-directionally forged 7075 aluminum alloy, Mater. Sci. Eng. A 700 (2017) 220–225.
[43] G. Bi, et al., Microstructure and mechanical properties of an extruded Mg-Dy-Ni alloy, Mater. Sci. Eng. A 760 (2019) 246–257.
[44] K. Wang, et al., Enhanced mechanical properties of Mg-Gd-Y-Zn-Mn alloy by tailoring the morphology of long period stacking ordered phase, Mater. Sci. Eng. A 733 (2018) 267–275.
[45] C.X. Ren, et al., Exploring the strength and ductility improvement of Cu–Al alloys, Mater. Sci. Eng. A 786 (2020) 139441.
[46] H. Mecking, U.F. Kocks, Kinetics of flow and strain-hardening, Acta Metall. 29 (1981) 1865–1875.
[47] G. Krauss, Martensite in steel: Strength and structure, Mater. Sci. Eng. A 273 (1999) 40–57.
[48] Y.Z. Tian, et al., Remarkable transitions of yield behavior and Lüders deformation in pure Cu by changing grain sizes, Scr. Mater. 142 (2018) 88–91.
[49] C. Keller, E. Hug, Kocks-Mecking analysis of the size effects on the mechanical behavior of nickel polycrystals, Int. J. Plast 98 (2017) 106–122.
[50] Y.Z. Tian, et al., A novel ultrafine-grained Fe–22Mn–0.6C TWIP steel with superior strength and ductility, Mater Charact 126 (2017).
[51] G. Dini, et al., Tensile deformation behavior of high manganese austenitic steel: the role of grain size, Mater. Des. 31 (2010) 3395–3402.
[52] C. Donadille, R. Valle, P. Dervin, R. Penelle, Development of texture and microstructure during cold-rolling and annealing of F.C.C alloys: Example of an austenitic stainless steel, Acta Metall. 37 (1989) 1547–1571.
[53] J.K. Kim, M.H. Kwon, B.C. De Cooman, On the deformation twinning mechanisms in twinning-induced plasticity steel, Acta Mater. 141 (2017) 444–455.
[54] Y. Ikeda, et al., Impact of interstitial C on phase stability and stacking-fault energy of the CrMnFeCoNi high-entropy alloy fcc hcp, Phys. Rev. Mater. 113603 (2019) 68–71.
[55] Z. Wang, et al., High stress twinning in a compositionally complex steel of very high stacking fault energy, Nat. Commun. 13 (2022) 1–8.
[56] M. Koyama, T. Sawaguchi, K. Tsuzaki, Deformation twinning behavior of twinning-induced plasticity steels with different carbon concentrations - Part 1: Atomic force microscopy and electron backscatter diffraction measurements, ISIJ Int. 55 (2015) 1747–1753.
[57] M. Koyama, T. Sawaguchi, K. Tsuzaki, Deformation twinning behavior of twinning-induced plasticity steels with different carbon concentrations - Part 2: Proposal of dynamic-strain-aging-assisted deformation twinning, ISIJ Int. 55 (2015) 1754–1761.
[58] M. Koyama, T. Sawaguchi, K. Tsuzaki, Influence of dislocation separation on dynamic strain aging in a Fe-Mn-C austenitic steel, Mater. Trans. 53 (2012) 546–552.